Size-dependent mechanical properties in AA6082 tailor welded specimens

Liu, Jun; Wang, Li-liang; Lee, Junyi; Chen, Ruili; El-fakir, Omer; Chen, Li; Lin, Jianguo; Dean, Trevor A.

DOI:
10.1016/j.jmatprotec.2015.05.004

Journal of Materials Processing Technology 224 (2015) 169–180

Contents lists available at ScienceDirect

Journal of Materials Processing Technology

journal homepage: www.elsevier.com/locate/jmatprotec

Size-dependent mechanical properties in AA6082 tailor welded specimens

Jun Liu [a], Li-Liang Wang [a,*], Junyi Lee [a], Ruili Chen [a], Omer El-Fakir [a], Li Chen [b], Jianguo Lin [a], Trevor A. Dean [c]

[a] Department of Mechanical Engineering, Imperial College London, London SW7 2AZ, UK
[b] Beijing Aeronautical Manufacturing Technology Research Institute, Beijing 100024, China
[c] School of Mechanical Engineering, The University of Birmingham, Edgbaston, Birmingham B15 2TT, UK

ARTICLE INFO

Article history:
Received 27 January 2015
Received in revised form 22 April 2015
Accepted 1 May 2015
Available online 12 May 2015

Keywords:
AA6082
Laser welding
Friction stir welding
HAZ
Global strength
Local strength

ABSTRACT

AA6082 tailor welded blanks (TWBs) produced using laser welding and friction stir welding were studied in this paper. The nominal mechanical properties of welded AA6082 under uniaxial tension conditions were characterised by evaluating the local properties of the base material, heat affected zone (HAZ) and weld zone. Tensile specimens were machined in the way that the weld line lies perpendicular to the loading axis. Three standard-sized specimens containing varying ratios of weld in the gauge region of the specimen were used to determine the size-dependent properties of welded AA6082 in the TWBs. A post-weld strength prediction (PWSP) model, based on the theories of plasticity, has been developed to estimate the post-weld properties of the tailor welded specimens. The model can be used to predict the post-weld yield strength and the global tensile behaviour of welded AA6082 specimens. Good agreements between the modelling and the experimental results have been obtained, with the yield strength deviation less than 6%. It was found that the yield strength increased with increasing dimensions of the tensile specimens. The size-dependent phenomenon was studied and the complex plastic deformation mechanisms have been found to cause the size-dependent phenomenon.

1. Introduction

Aluminium alloys are extensively used in the automotive and aerospace industries because of their excellent mechanical properties (Liu et al., 2010), such as high stiffness to density and high strength to density ratios. Due to the pressing demands for weight reduction and fuel efficiency in both land and air transportation, the usage of aluminium has been increasing rapidly in recent years, shrinking the discrepancy with the formerly overwhelming use of steels (Miller et al., 2000). Additionally, developments in advanced forming technologies, such as warm forming (Toros et al., 2008) and hot stamping (Mohamed et al., 2012), enable aluminium and its alloys (El Fakir et al., 2014) to be used in a wider range of applications.

Tailor welded blanks (TWBs) are single-piece semi-finished parts produced by joining sheets of the same or different gauge (Davies et al., 2002), or sheets of different alloys (Watanabe et al., 2006) using a variety of welding methods. In automotive industries, the use of TWBs as the lightweight structures continues to grow, increasing the importance of joining processes (Houldcroft et al., 1986). Typical joining technologies involve arc welding, tungsten inert gas welding (Tarng et al., 1999), laser beam welding (LBW) (Boukha et al., 2012), friction stir welding (FSW) (Chen and Kovacevic, 2004). Due to rapid developments in advanced forming technologies, it is now possible to form tailor welded blanks to produce a body panel with complex structure and reduced weight (Davies et al., 1999).

AA6082 tailor welded blanks using laser beam welding or friction stir welding are used in this study. Laser welding has various advantages, including high productivity, high weld quality in terms of controllable heat affected zone (HAZ) and weld zone, low distortion, flexibility due to the movable heat source, reliability and precision (Cao et al., 2003). However, aluminium alloys are one of the most challenging metals to be welded by laser, because of their high surface reflectivity, low molten viscosity and inherent oxide layer. In addition, minimising the HAZ in aluminium is more important than in other metals, in order to retain the mechanical properties of the parent material. Friction stir welding is a solid-state welding technique that is being developed to join parts comprising of either the same or different materials (Chen and

* Corresponding author. Tel.: +44 7883260966.
E-mail address: liliang.wang@imperial.ac.uk (L.-L. Wang).

http://dx.doi.org/10.1016/j.jmatprotec.2015.05.004

Kovacevic, 2004). It is an emerging technology that was introduced just over 20 years ago, and requires further research to assist its development for use in wider applications.

Researchers have found that the overall formability of TWBs is significantly affected by welding parameters, e.g. power source (Cao et al., 2003), welding speed (Liu et al., 2003), etc., especially for heat-treatable aluminium alloys. This is because different welding parameters result in different weld shapes, microstructures and temper conditions (Aydın et al., 2009), leading to significant variations in local mechanical properties (Zadpoor et al., 2007).

Generally, two types of specimens, longitudinal (weld line parallel to the tensile axis) and transverse (weld line perpendicular to the tensile axis) configurations, are utilised to evaluate the mechanical response of tailor welded blanks.

Tensile tests on tailor welded specimens with the weld lying parallel to the loading axis (Davies et al., 2000) suggested that characteristics of small specimens were able to consistently represent the properties of weld material in the TWBs. This is because small or miniature specimen sizes can increase the proportion of the weld metal in the gauge region (Ghoo et al., 2001); and thus sub-sized (non-standard) specimens were believed to give reliable tensile properties (Abdullah et al., 2001). AA2024 welded joints, accounting for 100% of the gauge region, have been assessed by micro-tensile test (Genevois et al., 2005). Genevois et al. (2006) further reported that, compared to the micro-tensile test, the standard tensile test perpendicular to the weld direction can represent the local mechanical properties of the monolithic weld obtained by the micro-tensile test as well. But because of the possible thermal or mechanical influences on the weld nugget during specimen preparation, it is difficult to produce a monolithic nugget specimen from the tailor welded blanks. Therefore, the standard specimen size can be used as a good substituent for the miniature specimen size when evaluating the weld properties.

Regarding the transverse weld configuration, Miles et al. (2004) evaluated tensile specimens with transverse weld line according to the ASTM standard (ASTM E8, 2013). Owing to the heterogeneous structures in the weldment, strain localisation in the transverse weld specimens has been observed at the interfacial region between the thermo-mechanically affected zone (TMAZ) and nugget (Lockwood et al., 2002). Digital image correlation (DIC) technique is able to map strain distributions of a tailor welded specimen, especially for the local stain at welded joints. Moreover, micro-grids that had been pre-marked on the weldment were utilised in a real-time microscopic recording system (Cheng et al., 2005). In this study, the deformation of the micro-grids clearly represented the local behaviour of the transverse joint during tension.

As complex deformation exists in welded specimens, numerical methods are deemed to be effective for evaluating the mechanical properties. The rule of mixtures (ROM) model has been conventionally introduced into the analysis of TWBs (Abdullah et al., 2001). Later studies using the ROM model revealed that the volume fraction of the weld zone in gauge area had significant effects on the global mechanical response of AA2024 friction stir welded specimens (Liu and Chao, 2005). However, the ROM model was a spring-in-series model, which assumed that the longitudinal strains are uniform across the welded specimen. It was not able to account for the plastic behaviour and capture the strain evolution theoretically in different zones of the tailor welded blanks. Finite element model utilising local constitutive behaviour for each local region has exhibited its capabilities in predicting global response of AA2024 friction stir welded specimens in terms of 2-D (Lockwood et al., 2002) and 3-D (Lockwood and Reynolds, 2003) elements. In fact, this model demonstrated good agreements with experiments, although it was based on a composite material approach (Genevois et al., 2006).

The aim of this research is to study size-dependent mechanical properties of laser welded and friction stir welded specimens with varying proportions of the parent material, weld zone and HAZ. The specimens were made according to different standards, and only transverse welded specimens were tested to investigate potential non-uniform deformation. A post-weld strength prediction (PWSP) model was also developed to help understand the mechanism of size effects on the global mechanical properties of AA6082 tailor welded specimens. This model, which incorporated the theories of plasticity applied to sheet metals, can simulate the welded specimens' time-dependent strain evolution during plastic deformation and predict their global strengths accurately.

2. Experimental details

2.1. Welding methods

The base material used in this study was the aluminium alloy AA6082-T6. Sheets with dimensions of 600 × 300 × 1.5 mm were initially tailored along the length (rolling) direction, and then were welded back together. Two welding methods, laser welding and friction stir welding (FSW), were used to evaluate and compare the post-weld properties.

Laser welding was carried out on the blanks using a Nd:YAG source through a 0.2 mm fibre with a power of 1.6 kW. The welding speed was 35 mm/s. For friction stir welding, the tailored blanks were butt-welded along the interface using a FSW machine. The tool rotation speed was 3000 rpm and its travelling speed was 7 mm/s. It is noted that only butt welds with fully penetrated joints have been studied in this work.

2.2. Uniaxial tensile tests

Tensile tests were carried out on an Instron 5584 to study the deformation characteristics of the localised areas in the TWBs at ambient temperature. Dog-bone shaped specimens were cut out perpendicular to the weld line from welded blanks. All the specimens were machined carefully with the centre lines of the weld zone and the specimen being coincident, as illustrated in Fig. 1.

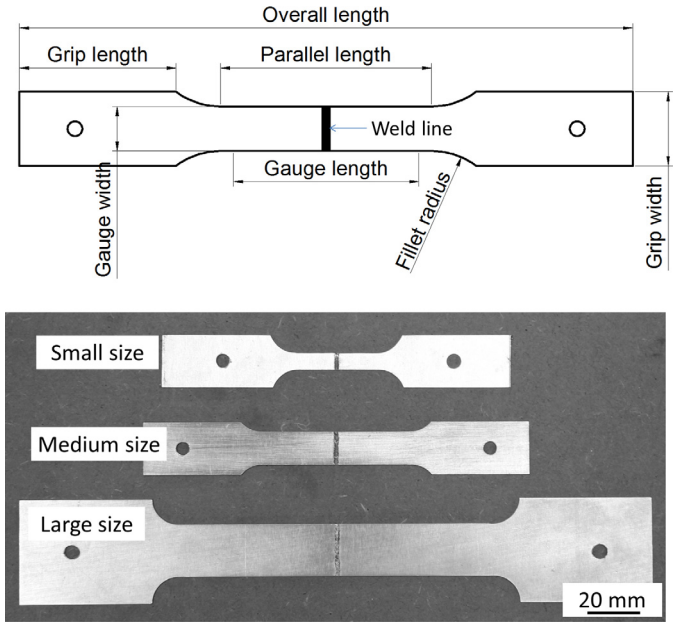

Fig. 1. Tensile specimen configurations.

Table 1
Specimen dimensions for tensile test (unit: mm).

	Small size (ASTM E8, 2013)	Medium size (ASTM E8, 2013)	Large size (ISO 6892, 2009)
Gauge length	25	50	80
Gauge width	6	12.5	20
Radius of fillet	10	20	20
Overall length	120	150	240
Parallel length	32	57	120
Grip length	40	40	50
Grip width	20	20	40

Three standard sizes, from ASTM E8 (2013) and ISO 6892 (2009) standards, were used to investigate the effect of specimen size on global strength of the welded specimens. All the dimensions are listed in Table 1. Constant crosshead speeds of 0.025, 0.05 and 0.08 mm/s were employed, for the three different gauge length specimens, respectively, with a corresponding initial strain rate of 0.001 s^{-1}. All the specimens were loaded until fracture by a load applied perpendicular to the weld line. Three tests for each specimen size have been performed and the tensile properties, which will be presented in Fig. 6, indicate good repeatability of the results.

2.3. Digital image correlation

Digital image correlation, an optical measuring method, was used to observe the local strain evolution during the tensile test. This method employs tracking and image registration throughout the test, and allows a measurement of displacement and strain to be made during deformation within localised regions. It can track the surface strain regardless of the thickness of the tested specimens.

Fig. 2 shows the typical data output from the DIC system during testing of a laser welded specimen. A black layer with white stochastic speckles overlaid was sprayed on the specimen surface, as shown in Fig. 2(a and b). The weld zone, HAZ and base metal zone have been distinguished by thickness values and hardness profiles (detailed in Section 3.1) prior to deformation. Subsequently, the local strains at these zones were determined using the DIC measurements, as shown in Fig. 2(c).

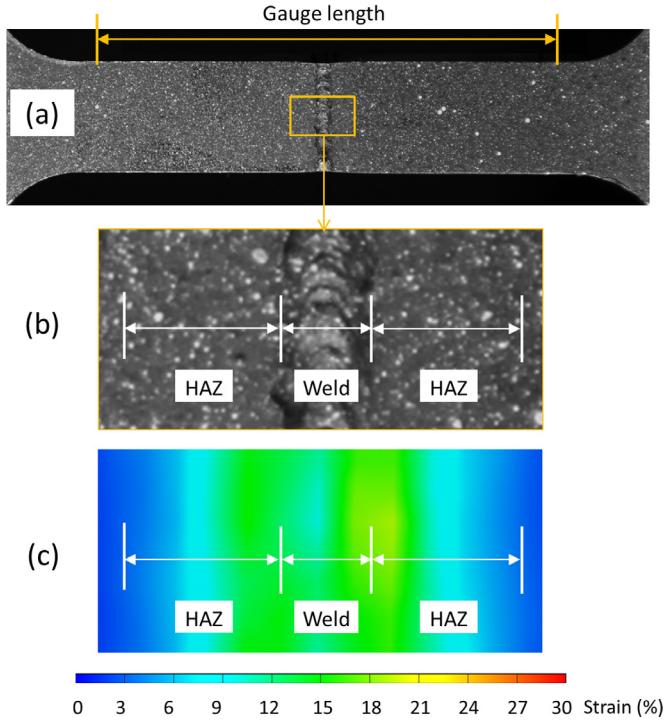

Fig. 2. (a) DIC tensile specimen, (b) zoomed-in specimen surface, and (c) strain field display of the specimen during tension.

In addition, the instantaneous force applied to the specimen was logged during the tensile test and the engineering stress was calculated by dividing the force by the corresponding initial cross-sectional area for each zone. Each dimension of the local zones is an average of three readings measured using a Vernier calliper. The geometric information is detailed in Section 3.1. The calculated local stress together with the measured local strain was used for characterisation of the local mechanical behaviour, i.e. the local stress–strain curve for each individual zone.

3. Experimental results

3.1. Determination of zones in TWB

The weld metal zone is the only zone where the metal is melted and solidified during laser welding. For friction stir welding, the weld metal is referred to as the stir zone where the tool probe rotates and heat is generated at the joint. Weld imperfections occurring at the cross-sections of the joints, e.g. excessive weld metal in laser welded blanks and tool marks in friction stir welded blanks, result in irregular and unsmooth segments on the weld bead. In addition, restraining forces imposed by clamps are applied in the horizontal (in plane) and vertical (in thickness) directions on the sheet metal being welded. Consequently, the weld metal only expands vertically (in thickness direction) due to volume expansion as heat is generated during welding. Thus, the welded joint produced after welding looks thicker compared to the base material. For simplification, the weld thickness, which was measured between the top and bottom surfaces of the weld bead, is assumed to be uniform as illustrated in Fig. 3.

The heat affected zone, which is present due to the heat conduction between the hot fusion metal zone (or the stir zone for FSW) and the un-deformed base metal zone, occurs in the base material. Thus, the thickness of the HAZ is identical to that of the base material, i.e. 1.5 mm. In addition to the HAZ, a thermo-mechanically affected zone exists in the friction stir welded blanks. In the thermo-mechanically affected zone, the material experiences both heating cycles and plastic deformation during welding. In order to characterise the different zones uniformly in the tensile specimens while simplifying potentially complex geometric problems, the TMAZ in

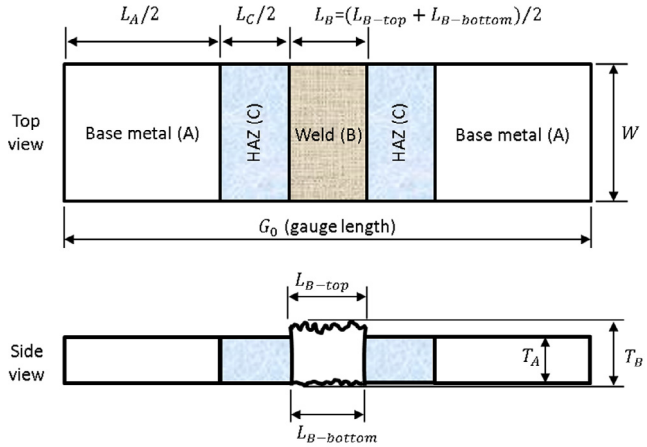

L_A - Length of base metal; L_C - Length of HAZ; T_A - Thickness of base metal (HAZ)

L_{B-top} - Weld length at top side; $L_{B-bottom}$ - Weld length at bottom side

L_B - Average weld length; W- Weld width (specimen width); T_B - Weld thickness

Fig. 3. Schematic of three zones in a welded specimen.

Table 2
Initial dimensions of three zones in the welded specimens (unit: mm).

	TWB specimen size	L_{A0}	L_{B0}	L_{C0}	T_{A0} (T_{C0})	T_{B0}
Laser welding	Small	16.82	1.88	6.3	1.51	1.67
	Medium	41.83	1.87	6.3	1.49	1.73
	Large	71.91	1.79	6.3	1.50	1.68
FSW	Small	9.19	7.31	8.5	1.50	1.57
	Medium	33.90	7.60	8.5	1.51	1.61
	Large	63.71	7.79	8.5	1.49	1.57

the friction stir welded specimens was considered to be part of the HAZ when determining the mechanical response.

The base metal zone outside the HAZ is unaffected and remains as the parent metal, maintaining the same mechanical properties as those existing prior to welding.

To determine the size and location of each zone, hardness tests were performed across the weld centre line using a Vickers Microhardness tester with a load of 200 g and a dwell time of 12 s. The hardness profiles for both welding conditions are plotted in Fig. 4, from which the typical three zones of the welded blanks can be distinguished clearly.

The hardness in the base metal zone remains the same (HV > 110) as that in the original state before welding. The heat affected zone exists physically and was determined by comparing the hardness profiles along the specimen length. The HAZ, located in between the base metal and the weld zone in Fig. 3, has varying hardness and strength along its length due to the occurrence of heat conduction (and plastic deformation for FSW) during welding. The hardness of the HAZ is highly non-uniform as shown in Fig. 4, which is a typical feature after welding. In general, the HAZs induced by both welding methods show increasing hardness towards the parent metal. However, for the friction stir welded blank, the trend of the hardness across each zone is different from that in the laser welded blank. The lowest hardness value was found in the HAZ, whereas for the laser welded blank it was in the weld zone.

Table 2 summarises the dimensions for individual zones in the TWB specimens. The cross-sections of the individual zones are not always in perfect rectangular shape, especially for the weld zone. As shown in Fig. 3, the weld surface structure is usually rough (with tool marks or patterns) and the weld cross-section has a trapezoid shape. The initial weld length, L_{B0}, is an average value measured from the top and bottom surfaces of the weld zone. It is deemed that the geometries of the weld or HAZ in the same tailor welded blank remain constant, although small variations were found in L_{B0} among different specimen sizes. The initial HAZ length, L_{C0}, was determined by comparing the hardness profiles in Fig. 4. As the tested specimens were machined from the same laser welded or friction stir welded blank, a constant HAZ length was used in the study. The initial length of base metal, L_{A0}, represents the remaining gauge region after deducting the corresponding weld and HAZ lengths. The weld thickness, T_{B0}, is measured between the top and bottom surfaces of the joint, as illustrated in Fig. 3. The initial thickness of the HAZ (T_{C0}) is assumed to be the same as that of the base metal (T_{A0}).

3.2. Tensile behaviour of welded specimens

Fig. 5 illustrates the representative engineering stress vs. engineering strain tensile curves for AA6082 before (unwelded parent AA6082-T6) and after welding, indicating decreased levels of tensile strength after welding. For the laser welded specimen, the ultimate tensile stress (UTS) is reduced by 33% after welding, compared to 25% in the friction stir welded specimen. The curves also show a significant decrease in ductility (global strain) after welding, from a ductility value of approximately 14% for the parent material to approximately 2% for the welded specimens. The strain variations of different zones in the welded specimens are discussed in Section 4.3.3.

Based on the observation of the local regions, it can be seen that the stress–strain curves of the HAZ and weld zone have different features. As shown in Fig. 5, the weld zone has the lowest strength. The HAZ of aluminium alloy welded blanks generally have an intermediate level of strength compared to the other two zones. By testing specimens of different sizes, proof strengths of specimens with the varying fractions of weld metal in the gauge length region were found, as shown in Fig. 6(a). The higher percentage of weld zone in the gauge length indicates a smaller tensile specimen, corresponding to the specimen size in Table 1. The data plots illustrate the global yield stress when the specimen gauge length used decreases from 80 mm (large size) to 25 mm (small size). The percentage of weld metal zone in the gauge length from the large size to the small size increases from 2.5% to 8% and 9.4% to 30%, for the laser welded and the friction stir welded specimens respectively. In this case, the global yield stresses reduce by 25% and 15%, respectively. It can be seen in Fig. 6(b) that, for the different sized specimens, no significant change in global ultimate tensile stress occurs for the welded specimens.

Compared to the decreasing trend of the global yield stress with increase in weld length to gauge length ratio, there are no significant size effects on the local strengths in the HAZ and weld zone. As the weld specimens were from the same tailor welded blank, the geometries of the welds and HAZ were identical respectively, although the gauge length has been changed. Therefore, constant stress–strain relationships for the local HAZ and local weld zone were employed respectively for the given conditions.

4. Post weld strength prediction model

4.1. Development of the PWSP model

The welding of aluminium blanks causes a significant decrease in the global strength of specimens due to the lower strengths of the weld metal zone and the HAZ. Although post-weld heat treatments can partially recover the strength of a heat-treatable aluminium alloy, because of thermal distortion, they are often not applicable for industrial components, especially those from the aerospace and automotive industries. Therefore, a post weld strength prediction (PWSP) model was developed to describe the degradation of material strength and to predict the effects of the geometries of the weld zone and HAZ on the global strength of the tailor welded specimens. A MATLAB based programme has been developed as a tool to implement the PWSP model in this study.

4.1.1. Constitutive equations

The developed model is based on the theory of plastic deformation and isotropic hardening in a material under plane stress. The coordinate system in this study follows the right hand rule with *Direction* 1 being the axial direction of the specimen, *Direction* 2 being the direction across the width of the specimen and *Direction* 3 being normal to the plane.

In this study, each zone was modelled as a single homogenous material undergoing loading under plane stress, ($\sigma_3 = 0$). Due to symmetry, the entire specimen in Fig. 3 can be fully described using only three sections, which are denoted by sections A, B and C for the base metal, the weld zone and the HAZ, respectively. A power law relationship, shown in Eq. (1) was used to describe the plastic deformation behaviour in the TWBs. The strength index (k)

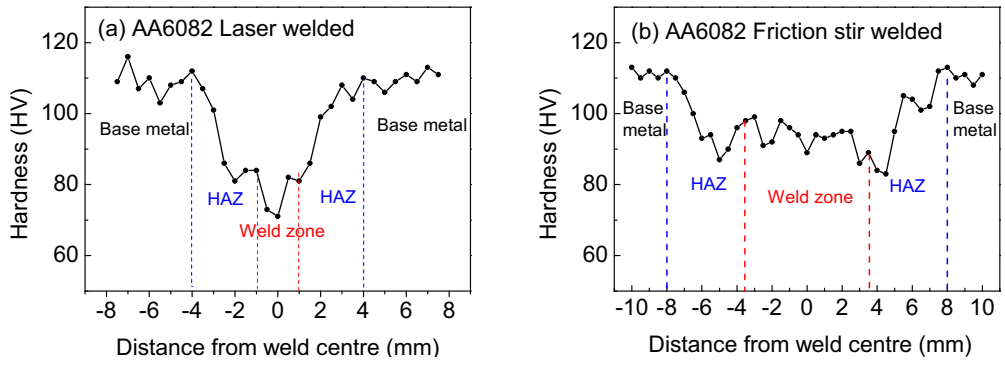

Fig. 4. Hardness profiles across the weld joints along the mid thickness of the blanks produced by (a) laser welding and (b) friction stir welding.

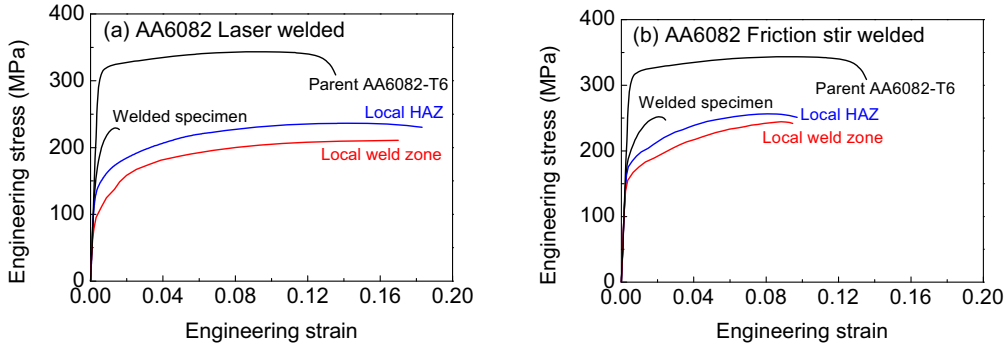

Fig. 5. Typical tensile curves for (a) laser and (b) friction stir welded specimens with a gauge length of 50 mm.

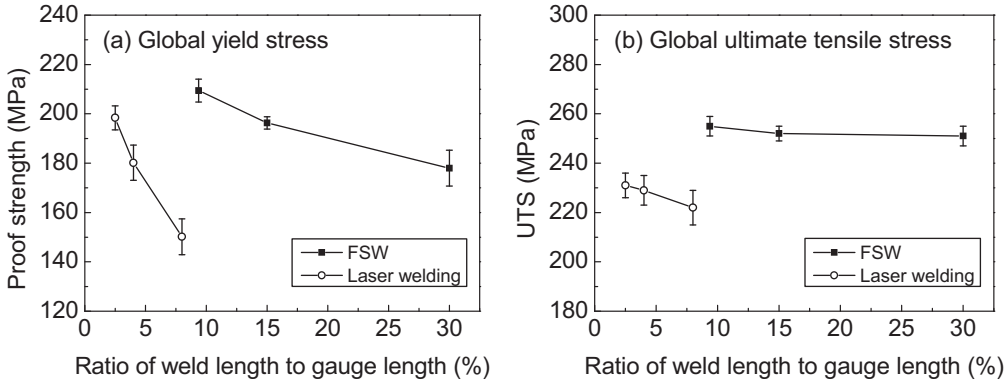

Fig. 6. Illustration of the effect of the percentage of weld metal in the gauge length on (a) global yield stress and (b) global ultimate tensile stress.

and strain hardening exponent (n) for each zone were determined experimentally,

$$\bar{\sigma} = \begin{cases} E\bar{\varepsilon}, & \bar{\varepsilon} \le \varepsilon_p \\ k\bar{\varepsilon}^n, & \bar{\varepsilon} > \varepsilon_p \end{cases} \quad (1)$$

where $\bar{\sigma}$ is the von-Mises equivalent stress, E is the Young's modulus, ε_p is the strain when yield occurs, k is the strength index and n is the strain hardening exponent, and $\bar{\varepsilon}$ is the equivalent strain in which the strain increments are described by Eq. (3).

$$\bar{\sigma} = \sqrt{\frac{1}{2}\left[(\sigma_1 - \sigma_2)^2 + \sigma_1^2 + \sigma_2^2\right]} \quad (2)$$

$$d\bar{\varepsilon} = \sqrt{\frac{2}{3}\left(d\varepsilon_1^2 + d\varepsilon_2^2 + d\varepsilon_3^3\right)} \quad (3)$$

The material was assumed to have constant volume and follows the Levy–Mises flow rule during plastic deformation as described by Eqs. (4) and (5) (Hosford, 2005), respectively. Additionally, a strain increment ratio, β, defined by Eq. (6) was introduced.

$$d\varepsilon_1 + d\varepsilon_2 + d\varepsilon_3 = 0 \quad (4)$$

$$\frac{d\varepsilon_1}{\sigma_1 - 1/3(\sigma_1 + \sigma_2 + \sigma_3)} = \frac{d\varepsilon_2}{\sigma_2 - 1/3(\sigma_1 + \sigma_2 + \sigma_3)} = \frac{d\varepsilon_3}{\sigma_3 - 1/3(\sigma_1 + \sigma_2 + \sigma_3)} \quad (5)$$

$$\beta = \frac{d\varepsilon_2}{d\varepsilon_1} \quad (6)$$

The Young's modulus, E, in this study for all three materials was set to 70 GPa. It is noted that the terms in Eqs. (1)–(6) represent the true stress and true strains.

4.1.2. Boundary conditions

In this study, the base metal zone (Zone A) was assumed to be undergoing uniaxial tension as no stresses were applied in *Direction* 2 and 3 for the base metal zone, and the stress in *Direction* 2 exerted by the HAZ on the base metal is considered to be small compared to the stresses in the axial (*Direction* 1). For uniaxial tension in the base metal, the strain increment ratio, β_A, where the subscript denotes the zone, is equal to −0.5. The axial strain in Zone A, ε_{1A}, is the independent variable that is used as an input. The strains in *Direction 2* and *3* and the stress in *Direction* 2 can be found by solving Eqs. (1)–(6).

The material in Zone C (HAZ) was assumed to undergo plane stress. The stresses and strains were calculated by setting the boundary conditions to fulfil force balance and strain continuity conditions across the width for the material defined by Eqs. (7) and (8), respectively, since Zone C is adjacent to Zone A.

$$\sigma_{1C} = \frac{W_A T_A}{W_C T_C}\sigma_{1A} \tag{7}$$

$$d\varepsilon_{2C} = d\varepsilon_{2A} \tag{8}$$

where W and T are the real-time width and thickness of the individual zones, respectively.

The stresses and strains for the material in Zone B (weld zone) were calculated in a similar manner as the material in Zone C as seen in Eqs. (9) and (10) using the calculated values of the stresses and strains in Zone C. Additional zones can be added by following the same procedure.

$$\sigma_{1B} = \frac{W_C T_C}{W_B T_B}\sigma_{1C} \tag{9}$$

$$d\varepsilon_{2B} = d\varepsilon_{2C} \tag{10}$$

In this model, zones B and C were assumed to have uniform strains for the individual zones as the strains distribution observed during the tensile test, as seen in Fig. 2, appears to be uniform.

4.1.3. Numerical calculations

Numerical integration was applied to Eqs. (1)–(10) in order to calculate the stresses and strains in each zone for the global stresses and strains of the welded specimens. In this study, the central difference method was used for the numerical integration and Eqs. (1)–(10) were expressed in terms of their current values and increments. However, for the sake of brevity the numerical scheme is not described in detail here.

In the numerical calculations, the increments of strain $\Delta\varepsilon_{2A}$, $\Delta\varepsilon_{3A}$ and $\Delta\sigma_{1A}$ were first calculated using values of the previous step, the strain increment in *Direction* 1 in Zone A, $\Delta\varepsilon_{1A}$, and setting β_A to −0.5. After that, using the calculated values of $\Delta\varepsilon_{2A}$ and $\Delta\sigma_{1A}$, the values of $\Delta\varepsilon_{1C}$, $\Delta\varepsilon_{3C}$, $\Delta\sigma_{1C}$ and $\Delta\sigma_{2C}$ were calculated using Newton–Raphson iteration for β_C. The values of $\Delta\varepsilon_{1B}$, $\Delta\varepsilon_{3B}$, $\Delta\sigma_{1B}$ and $\Delta\sigma_{2B}$ were then calculated in a similar manner using the calculated values of $\Delta\varepsilon_{2C}$ and $\Delta\sigma_{1C}$. The stresses and strains were updated accordingly and these steps were then repeated for the next increment for the entire simulation. The procedure for the numerical calculations is illustrated in the flow chart in Fig. 7.

The stresses and strains were recorded and the global engineering stress, δ, and engineering strain, e_n, for the entire specimen were calculated using the following equations:

$$\delta_n = \frac{\delta_{A,n} W_{A,n} T_{A,n}}{W_{A,0} T_{A,0}} \tag{11}$$

$$e_n = \frac{\left(L_{A,n} + L_{B,n} + L_{C,n}\right) - \left(L_{A,0} + L_{B,0} + L_{C,0}\right)}{L_{A,0} + L_{B,0} + L_{C,0}} \tag{12}$$

where n denotes the increment number.

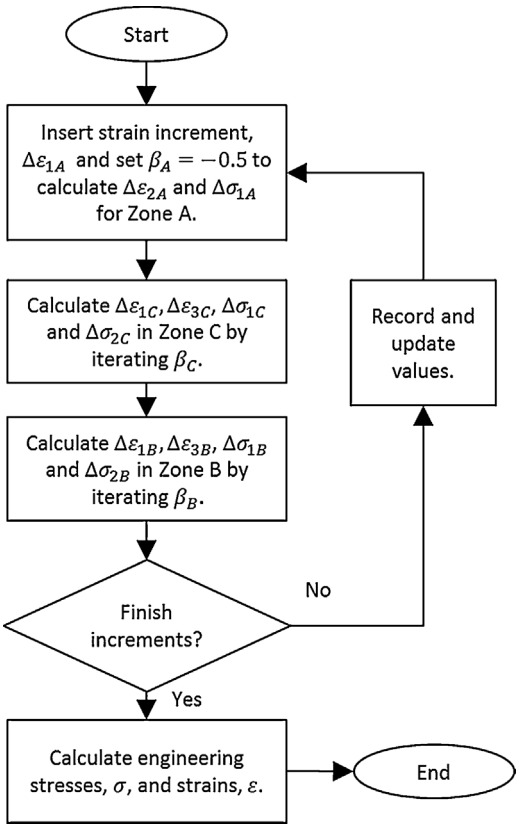

Fig. 7. Flow chart for the PWSP model. Zone A, B and C represent base, weld and HAZ areas corresponding to Fig. 3.

An important point to note here is that the lengths, width and thickness in Eqs. (11) and (12) are updated at every increment as seen in the following equations:

$$W_n = W_{n-1} + \Delta\varepsilon_{2,n}(W_{n-1}) \tag{13}$$

$$T_n = T_{n-1} + \Delta\varepsilon_{3,n}(T_{n-1}) \tag{14}$$

$$L_n = L_{n-1} + \Delta\varepsilon_{1,n}(L_{n-1}) \tag{15}$$

4.2. Application of the PWSP model

4.2.1. Calibration of local stress–strain curves

The laser welded AA 6082 specimens were measured to have a weld length (L_{B0}) of approximately 2 mm and a joint thickness (T_{B0}) of 1.68 mm. The exact dimensional values for each specimen were obtained individually. The length of the HAZ was estimated to be about 3.15 mm ($L_{C0}/2$) on each side of the weld by comparing with the hardness gradient.

During calibration, a power law relationship was used to describe the plastic stress–strain behaviour for all three zones. As stated in Section 3.2, there are no size effects on the strengths of the local HAZ and weld zones in tailor welded blanks, because unlike the entire specimen that possesses regions with different material properties, the material properties at the local scale is uniform. All the material constants for the three zones (base metal, HAZ and weld zone) of the welded specimens are given in Table 3. The material model using the power law coefficients (solid lines) has been compared to the experimental stress–strain curves (symbols) as shown in Fig. 8. Good agreement was achieved in the calibration of the local tensile curves of the HAZ and weld zone, validating the estimations of k and n, respectively. The calibration to obtain the material parameters for the individual zones was performed using the stress–strain behaviour of the individual zones obtained using

Table 3
Material constants for the local zones used in the PWSP model.

	Power law coefficients	Base zone	HAZ	Weld zone
Laser welding	E (GPa)	70	70	70
	K (MPa)	373	338	302
	n	0.033	0.17	0.18
FSW	E (GPa)	70	70	70
	K (MPa)	373	400	355
	n	0.033	0.175	0.16

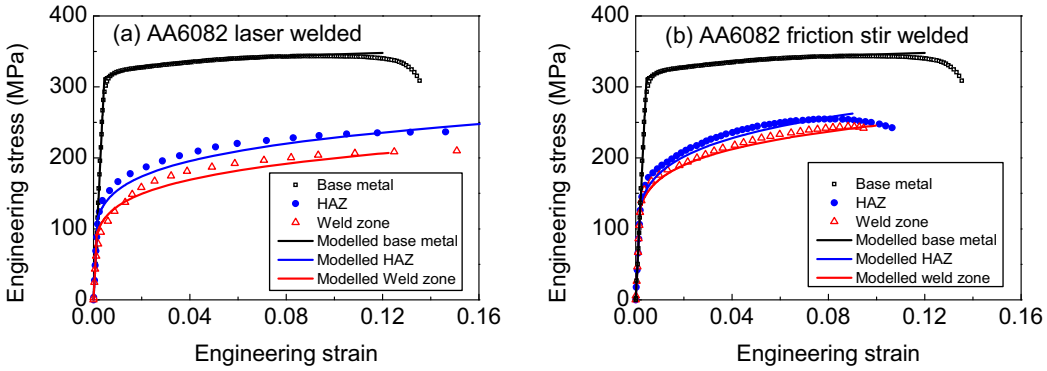

Fig. 8. Calibration of the tensile curves for local zones between modelling (solid lines) and experiment (symbols).

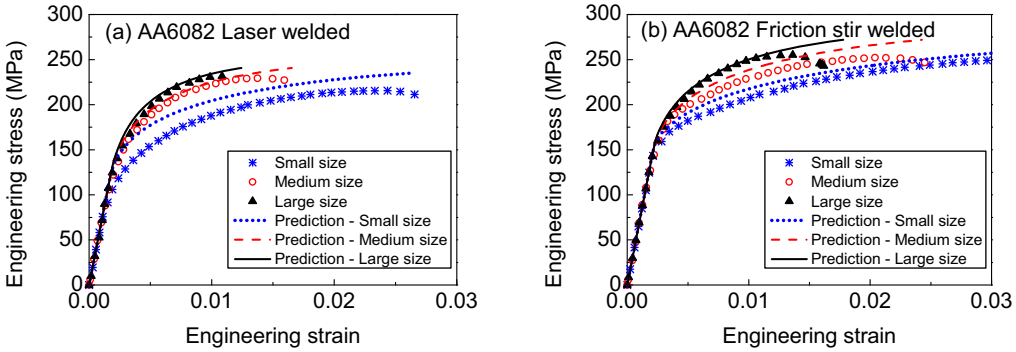

Fig. 9. Comparison of size-dependent stress–strain curves between prediction (lines) and experiment (symbols) in AA6082 tailor welded specimens.

DIC. Therefore the parameters for each individual zone in Fig. 8 were validated individually. The calibrated engineering data have been converted to true values for calculations in the PWSP model.

4.2.2. Prediction of the global strength

Geometries of the three zones, the estimated strength indexes and the strain hardening exponents (Table 3) were input into the PWSP model. The predicted stress–strain curves were compared with the global tensile behaviour of the welded specimens and shown in Fig. 9. The experimental data is depicted by symbols. The strains and corresponding stresses calculated using the PWSP model are plotted in solid lines. The 0.2% offset yield stress values from the prediction model and the experimental results are given in Table 4. The comparisons verified the accuracy of the model in predicting the global flow stress as well as the 0.2% proof strength of AA6082 tailor welded specimens, as the deformation behaviour of the material was predicted accurately. For the small sized specimen, the model predicts a yield stress of 172 MPa, overestimating the tested proof strength (150 MPa) by 12.8%. The deviation decreases to 2.5% in predicting the yield stress under the same welding condition, but with a larger gauge length. The possible sources of error will be discussed in Section 4.3.1.

The PWSP model was further verified by comparing the global strength prediction with the experimental data for friction stir welded specimens, as shown in Fig. 9(b). The specimen measured has a weld length (L_{B0}) of 7.6 mm and a thickness (T_{B0}) of 1.61 mm. The weld strength index and strain hardening exponent was estimated to be 355 MPa and 0.16, respectively. As with the laser welded specimens, a similar power law relationship with the corresponding material coefficients was then implemented into the PWSP model. The total HAZ length (L_{C0}) here is about 8.5 mm, larger than that (6.3 mm) of the laser welded blank. The HAZ has a slightly higher local strength compared to the weld zone, with the values of k and n being 400 MPa and 0.175, respectively, as provided in Table 3.

4.3. Discussion and capabilities of the PWSP model

4.3.1. Deviation analysis

4.3.1.1. Geometric complexity. The global tensile behaviour of welded specimens with various sizes has been predicted by the PWSP model, showing good agreements with experimental data. The tensile TWB specimen was divided into three zones: base metal, heat affected zone and weld zone. In the model, the cross-sections of all the three zones are assumed to have a rectangular shape, as shown in Fig. 3. This may not always be very accurate, especially for the friction stir welded blanks, where the cross-sections of the three zones may vary due to the process parameters (Ren et al.,

Table 4
Size-dependent yield stress in AA6082 tailor welded specimens.

	Specimen size	Ratio of weld length to gauge length (%)	Global 0.2% yield stress (MPa)	Modelling (MPa)	Deviation (%)
Laser welding	Small	8	150	172	12.8
	Medium	4	180	191	5.8
	Large	2.5	198	202	2.0
FSW	Small	30	178	188	5.3
	Medium	15	196	205	4.4
	Large	10	209	215	2.8

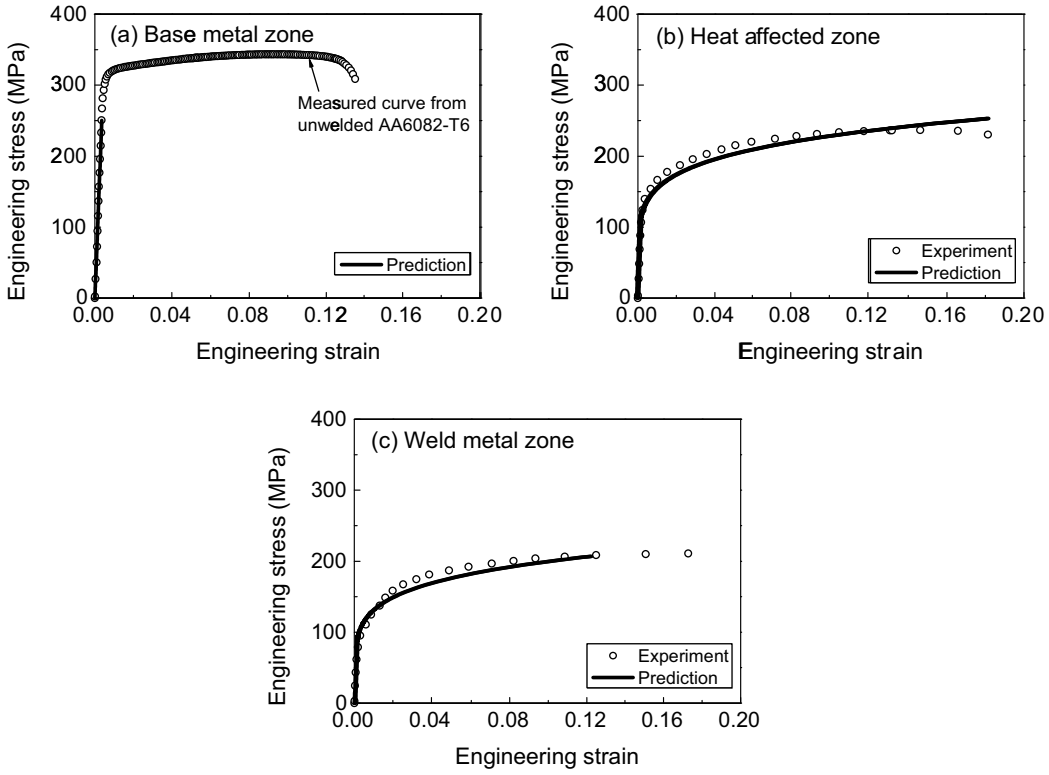

Fig. 10. Typical local tensile curves for three zones: (a) base metal, (b) HAZ, and (c) weld zone in a laser welded specimen showing the stress status during tension. Symbols are from experiment, while solid lines from the PWSP model.

2007) and temperature variations (Mahoney et al., 1998). In reference (Mahoney et al., 1998), the weld zone cross-section for friction stir welded specimens is actually described as being V-shaped. A non-rectangular cross-sectional shape can contribute to off-axis loading during tension and affect the measured results. However, as the model was able to predict the flow stress accurately, see Table 4, the influence of the geometric complexity is likely to be small.

4.3.1.2. Inhomogeneous deformation. Furthermore, another assumption is the homogeneous deformation within each local zone during calibration of the material constants (Table 3) and the prediction of the local mechanical response. However, this is not the case in practice as the strains are non-uniformly distributed across the entire gauge length. Fig. 10 shows the predicted local tensile curves for the three zones in a laser welded specimen during tension. The solid lines represent the predicted curves, while the symbols are the measured stress–strain curves for the local zones. According to the model prediction, the base metal was still deforming within the elastic region, while the material at the HAZ and weld zone have yielded.

Nevertheless, on the basis of the hardness profile in Fig. 4, the hardness values are not constant across the HAZ and weld zone, suggesting strength gradients in the regions. The two zones would therefore be inhomogeneous under tensile loading, compared to the base metal which is largely homogeneous in strength. As deformation progressed, strains accumulated locally in the interface between weld zone and HAZ, as observed in Fig. 11, where the

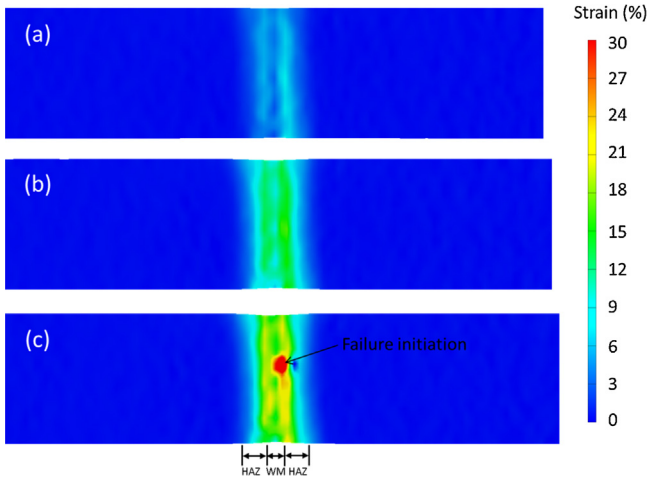

Fig. 11. DIC strain distributions of a laser welded specimen at different localised strain (ε_{max}) states: (a) ε_{max} = 0.08, (b) ε_{max} = 0.16, and (c) ε_{max} = 0.38.

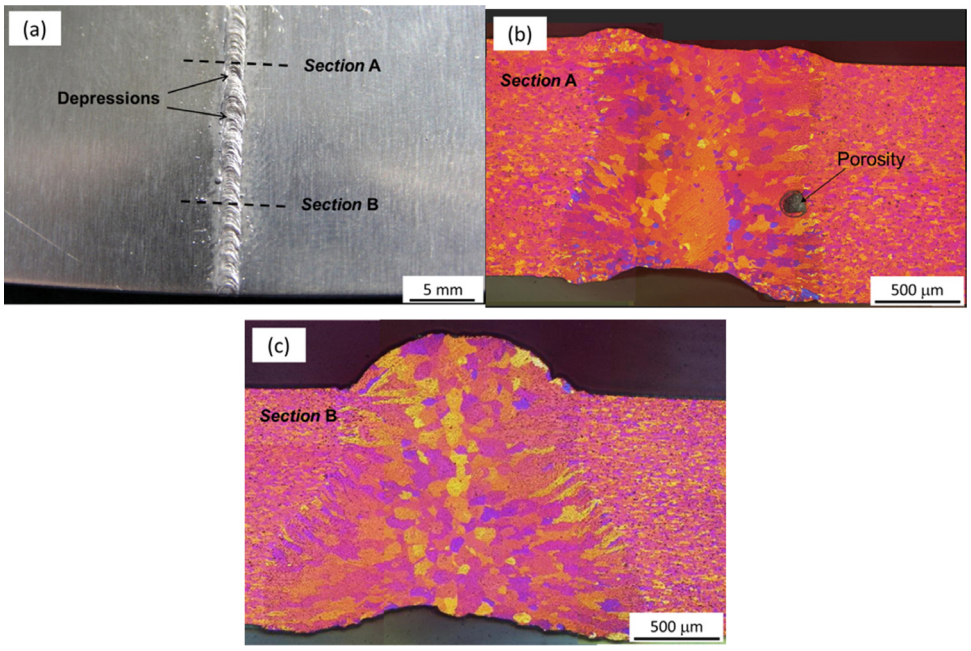

Fig. 12. (a) Top view of the laser welded blank, (b) cross-sectional microstructure of the laser welded blank showing porosity existing in the butt joint, and (c) cross-sectional microstructure of the laser welded blank showing good weld bead.

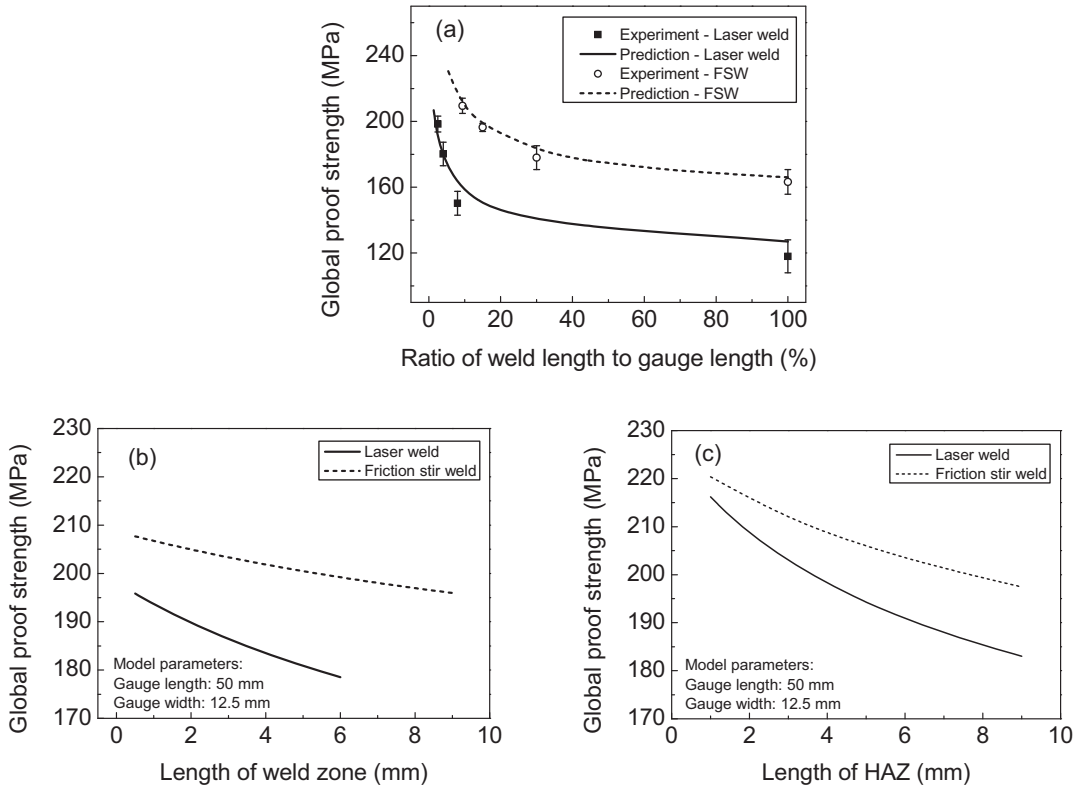

Fig. 13. (a) Effect of the fraction of weld metal on global proof strength, (b) predicted 0.2% yield stress of welded specimens with different weld zone lengths, and (c) predicted 0.2% yield stress of welded specimens with different HAZ lengths.

localised strain in the HAZ was clearly much higher than the other areas in the same zone.

4.3.1.3. Weld imperfection. Imperfections in the weld metal have also been attributed as a possible cause of the deviation between the predictions and experimental results. This factor can explain the significant decrease of stress level in the small-sized laser welded specimen in Fig. 9(a). The imperfections may come from the surface irregularities or internal pores that formed during solidification of the weld metal, particularly in the laser welded blanks.

The spaced valleys or depressions at the weld bead are clearly visible in Fig. 12(a) for a laser welded blank. In order to minimise the error induced by the surface imperfections, all the tensile specimens were selected and machined from regions in the TWB without

visible surface irregularities (e.g. depressions near *section* A). Only specimens where no visible surface defects on the weld bead could be seen (e.g. around *section* B) were tested in the study.

Fig. 12(b) shows that the welded joint at *section* A (near the depression) is thinner than the parent material. The pores, adjacent to the interface, would have also reduced the cross-sectional area in the deformation region, leading to a reduced reaction stress. It is difficult to quantify the impacts of the porosity on the welding performance in this case as their number is unknown, but it is believed that they were present in very few specimens.

Fig. 12(c) is the optical microstructure of the butt joint observed from *section* B of the TWB. The joint area, which has been assessed in this study, is thicker in comparison to the material in the surrounding area (base material). Fig. 12(b and c) also show that various sized grains exist in the centre of the weld bead, and columnar grains towards the weld/HAZ interface. The grain size in the weld bead is not ideal for achieving the best mechanical properties. The irregularity in the surface and microstructure as well as the interval pores cannot be eliminated easily due to the nature of laser welding aluminium alloys. It is not realistic to attempt to model most of these features which are random and inconsistent.

4.3.2. Size-dependent global mechanical properties in tailor welded specimens

For a given set of welded blank parameters, as listed in Table 3, the global mechanical properties including the proof strength can be calculated using the PWSP model. It takes into account the variations of mechanical behaviour in welded specimens of various sizes. Theoretically, it is applicable to specimens made using any type of welding method and any type of aluminium alloy as the only inputs required are weld dimensions, strength indexes and the strain exponents. One of the most promising applications of this model is to predict global proof strengths of welded specimens with different weld (or HAZ) zone sizes. The size effects can be attributed to the effective localised deformation within the weld and HAZ zones, as shown in Fig. 11.

Fig. 13(a) shows two curves representing the trends of global proof strength with respect to the fraction of the weld metal in the measured gauge region. The smaller fraction value corresponds to a larger specimen length, while a value of 100% means that the entire specimen is made of weld zone material. The decreasing trend with increasing weld fraction shows a significant reduction in global proof strength as the fraction of the weld length (L_{B0}) increases to around 40% of the gauge length. The yield stress decreases with increasing weld zone fraction until it reaches a value close to that of the weld metal. This observation suggests that the fraction of the weld metal in the gauge length is an important factor influencing the global properties of the welded AA6082, and this can be predicted correctly using the PWSP model.

By fixing the specimen size (gauge length and gauge width), the PWSP model is able to predict the global mechanical response of welded specimens with varying weld geometries individually. As shown in Fig. 13(b), the 0.2% proof strengths are predicted, indicating a decreasing trend with increasing weld length (L_{B0}). In this figure, the HAZ length (L_{C0}) has been fixed as 6.3 and 8.5 mm, respectively, for laser welding and FSW.

Similar to the effect of weld metal length, in Fig. 13(c) two curves are plotted in relation to HAZ length (L_{C0}). Constant values of 2 and 7.5 mm of the weld length (L_{B0}) for laser welding and FSW were used according to measurements on specimens. Both Fig. 13(b) and (c) reveal that the laser welded specimen had a lower strength compared to that of the friction stir welded specimen. This also is caused by the decrease in strength of the weld zone after the laser welding process. Therefore, in the welding process, the global properties of welded specimen can be enhanced by reducing the fraction of the weld zones in gauge region and/or by increasing the strength of the joint material.

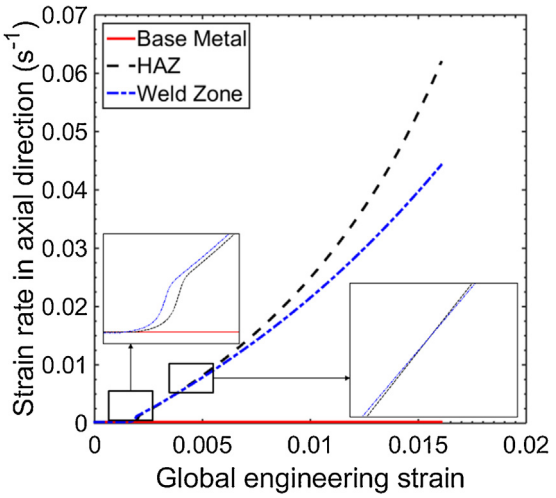

Fig. 14. Strain rate in the axial direction vs. global engineering strain of the medium size laser welded specimen.

The variations in global proof stress in tailor welded specimens as discussed in this study are a result of several mechanisms that are present during deformation, such as the lower local strength in the HAZ and weld zone, localised straining of the individual zones and variations in their geometry. Since the stress state and changes in geometry of the individual zones are calculated in the model throughout the entire deformation, the model is capable of explaining some of the mechanisms that contribute to the global stress–strain behaviour observed in the experimental data. For example, the observation that all welded specimens in this study fractured in the HAZ, despite the HAZ being significantly stronger than the weld zone as seen in Fig. 8.

4.3.3. Deformation characteristics

Fig. 14 shows strain rate evolutions of the individual zones in the axial direction at different global engineering strains for the medium size laser welded specimen over the loading duration. The values in Fig. 14 were calculated using the PWSP model up to the point where the global strain was equal to the failure strain measured from the experiments. As seen in Fig. 14, at the start of the loading, the HAZ and base metal have the same initial strain rate ($0.001\,s^{-1}$), as all the zones are undergoing elastic deformation. When the global strain is around 1.6×10^{-3}, the weld zone starts to yield followed closely by the HAZ, exhibiting significantly increased strain rate, as seen from the zoomed in figure in Fig. 14. Additionally, during the plastic deformation of the HAZ and weld zone, the gradient of the curve (strain rate) for the base metal in Fig. 14 was found to be constant. This also indicated the raising trends in the strain rate at the HAZ and weld zone as tension progressed gradually dominated the global deformation, contributing a larger proportion of the global strains.

The thickness of the material in the HAZ and weld zones during plastic deformation will also reduce significantly compared to the base metal, which is still undergoing elastic deformation, as shown in Fig. 15. Furthermore, as shown in Fig. 14, the weld zone will maintain a slightly larger strain rate compared to the HAZ from the onset of yielding until an global strains of approximately 3.5×10^{-3}. The strain rate in the HAZ then begin to increase above the weld zone, and continue to increase at a higher rate compared to the weld zone. The variations in stress at each zone can lead to variations in strain as well as in the strain rate. The model predicts that the deformation features of welded specimen is caused by a

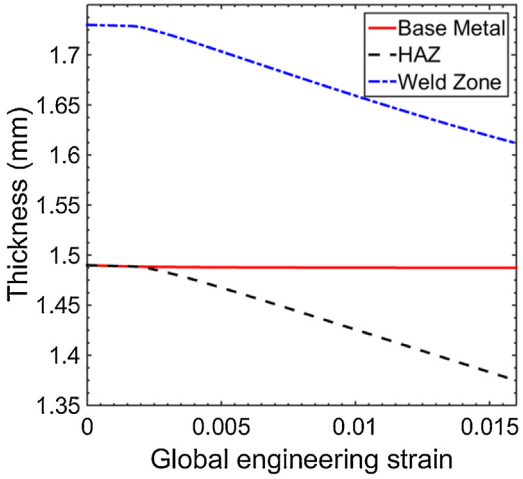

Fig. 15. Thickness vs. global engineering strain of the medium size laser welded specimen.

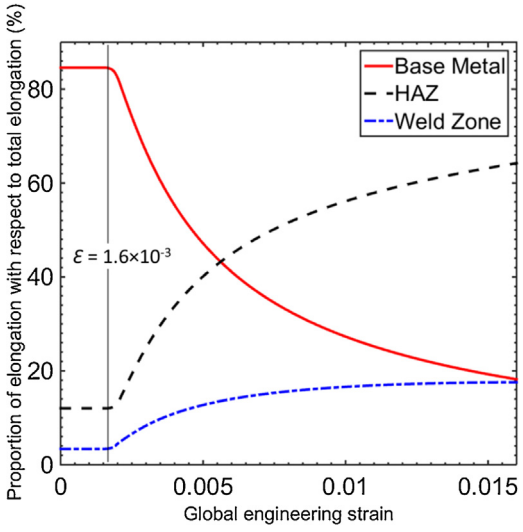

Fig. 16. Proportion of elongation of the individual zones with respect to the total elongation vs. global engineering strain curve for the medium size welded specimen.

combination of the different local plastic behaviour, the original difference in geometry, and further changes, such as strain rate and thickness evolutions in the three zones.

Additionally, the global stress–strain response of the entire specimen and hence the proof stress of the entire material are also affected by all the stated effects, especially localised straining of the HAZ. Fig. 16 shows the proportion of elongation of the individual zones defined here as the rate of change of the length in the individual zones over the rate of change of the overall length, as shown in Eq. (16). The proportion of elongation represents the contribution of each individual zone to the increase in length of the entire specimen.

$$\text{Proportion of elongation} = \frac{dL_{\text{Zone}}}{dL_{\text{Overall}}} \tag{16}$$

As shown in Fig. 16, during elastic deformation at global strain below 1.6×10^{-3}, the proportion of elongation for each material stays constant with the base metal contributing the most to the elongation of the entire specimen. This result is expected as the stiffness of all three zones is constant during elastic deformation and the length of the base metal is the largest. The proportion of elongation for the weld zone during initial deformation in Fig. 16 is less than its percentage in length as the weld zone is thicker than the HAZ and base metal zones. During plastic deformation of the HAZ and weld zones, the proportion of elongation for both of these zones increases significantly while the proportion of elongation for the base metal decreases significantly and is almost equal to the weld metal when the material fractures, despite the base metal having the largest proportion of length. This is because the HAZ and weld zone experience significantly larger strains compared with the base metal, which is still elastically deforming with a very slow strain rate (2×10^{-4}) as seen in Fig. 14. The significant decrease in thickness of both the HAZ and weld zones compared to the base zone in Fig. 15 also contributes to the increase in the proportion of elongation at these zones. Additionally, the proportion of elongation of the HAZ in Fig. 16 was found to be the largest during the entire loading, contributing to more than 60% of the increase in global length towards the end of the loading. This result is consistent with the DIC results shown in Fig. 11 and it suggests that the main deformation strains are localised in the HAZ.

Therefore, HAZ is an important factor impacting the global strain and the 0.2% offset yield stress. For instance, a larger increase (11.7% for FSW) of proof strength can be seen as the HAZ length (L_{C0}) reduces from 9 to 1 mm in Fig. 13(c), compared to 5.6% when decreasing the weld length (L_{B0}) in Fig. 13(b). Significant enhancement in the strength could be achieved if appropriate weld dimensions are obtained during welding. In the present research, only one set of constant welding parameters were used, thus the local strength of the weld zone and HAZ was constant. However, changing the welding parameters could not only affect the geometries, but also the local strengths of individual zones. The optimisation of welding parameters is therefore a complex scientific task and computationally expensive, which also requires much more experimental results. However, the PWSP model introduced in this paper is capable of simulating all these complex mechanisms with low computation effort, and accurate calculations for a large number of parameters can be performed rapidly using the PWSP model. This model could be further developed to predict the strengths of longitudinal welded specimens (weld line parallel to the loading axis) as well as full-scale tailor welded blanks.

5. Conclusions

Local mechanical properties obtained from tensile tests and measured using DIC techniques have determined the size-dependent effects and stress–strain relationships of AA6082 tailor welded specimens. The weld metal zone and HAZ in the welded blanks play an important role in the mechanical response to tensile loads. The results revealed an increased global proof stress level with a decreased fraction of weld zone in the gauge region of the specimens. Inhomogeneous strength and variable weld geometries have resulted in non-uniform strain distributions within the individual zones, showing the complex nature of the plastic deformation characteristics.

A post-weld strength prediction model has been developed that can be used to obtain detailed understanding of the complex plastic deformation mechanisms of tailor welded specimens. It has been validated to predict the global flow stress curves as well as the 0.2% proof strength of welded AA6082 with reasonable deviation, as low as 2.0% for laser welding and 2.8% for friction stir welding. The local strengths and dimensions of the weld zone and HAZ in the measured gauge region are the major factors influencing the global properties of the welded specimens.

Acknowledgements

The financial support from Innovate UK, Ultra-light Car Bodies (UlCab, reference 101568), is gratefully acknowledged. The authors would like to appreciate Dr. Sam Wei at the TWI Technology Centre, Yorkshire, for making the friction stir welded specimens. Thanks are also given to Innoval Technology Limited for performing microstructural analysis. Significant support was also received from the AVIC Centre for Structural Design and Manufacture at Imperial College London, which is funded by Aviation Industry Corporation of China (AVIC).

References

Abdullah, K., Wild, P.M., Jeswiet, J.J., Ghasempoor, A., 2001. Tensile testing for weld deformation properties in similar gage tailor welded blanks using the rule of mixtures. J. Mater. Process. Technol. 112, 91–97.

ASTM E8, 2013. Standard Test Methods for Tension Testing of Metallic Materials.

Aydın, H., Bayram, A., Uğuz, A., Akay, K.S., 2009. Tensile properties of friction stir welded joints of 2024 aluminum alloys in different heat-treated-state. Mater. Des. 30, 2211–2221.

Boukha, Z., Sánchez-Amaya, J.M., Amaya-Vázquez, M.R., González-Rovira, L., Botana, F.J., 2012. Laser welding of aeronautical and automobile aluminum alloys. AIP Conf. Proc. 1431, 974–981.

Cao, X., Wallace, W., Poon, C., Immarigeon, J.P., 2003. Research and progress in laser welding of wrought aluminum alloys. I. Laser welding processes. Mater. Manuf. Process. 18, 1–22.

Chen, C.M., Kovacevic, R., 2004. Joining of Al 6061 alloy to AISI 1018 steel by combined effects of fusion and solid state welding. Int. J. Mach. Tool Manuf. 44, 1205–1214.

Cheng, C.H., Chan, L.C., Tang, C.Y., Chow, C.L., 2005. Determination of true stress–strain curve for the weldment of aluminum laser-welded blanks. J. Laser Appl. 17, 159–170.

Davies, R.W., Oliver, H.E., Smith, M.T., Grant, G.J., 1999. Characterizing Al tailor-welded blanks for automotive applications. JOM 51, 46–50.

Davies, R.W., Smith, M.T., Khaleel, M.A., Pitman, S.G., Oliver, H.E., 2000. Weld metal ductility in aluminum tailor welded blanks. Metall. Mater. Trans. A 31, 2755–2763.

Davies, R.W., Vetrano, J.S., Smith, M.T., Pitman, S.G., 2002. Mechanical properties of aluminum tailor welded blanks at superplastic temperatures. J. Mater. Process Tech. 128, 38–47.

El Fakir, O., Wang, L., Balint, D., Dear, J.P., Lin, J., Dean, T.A., 2014. Numerical study of the solution heat treatment, forming, and in-die quenching (HFQ) process on AA5754. Int. J. Mach. Tool. Manuf. 87, 39–48.

Genevois, C., Deschamps, A., Denquin, A., Doisneau-cottignies, B., 2005. Quantitative investigation of precipitation and mechanical behaviour for AA2024 friction stir welds. Acta Mater. 53, 2447–2458.

Genevois, C., Deschamps, A., Vacher, P., 2006. Comparative study on local and global mechanical properties of 2024 T351, 2024 T6 and 5251 O friction stir welds. Mater. Sci. Eng. A 415, 162–170.

Ghoo, B.Y., Keum, Y.T., Kim, Y.S., 2001. Evaluation of the mechanical properties of welded metal in tailored steel sheet welded by CO_2 laser. J. Mater. Process Technol. 113, 692–698.

Hosford, W.F., 2005. Mechanical Behavior of Materials. Cambridge University Press.

Houldcroft, P.T., Feng, Fim, Fweldi, 1986. Welding process developments and future trends. Mater. Des. 7, 162–169.

ISO 6892, 2009. Metallic Materials – Tensile Testing. Part 1: Method of Test at Room Temperature.

Liu, H.J., Fujii, H., Maeda, M., Nogi, K., 2003. Tensile properties and fracture locations of friction-stir-welded joints of 2017-T351 aluminum alloy. J. Mater. Process Technol. 142, 692–696.

Liu, J., Tan, M.J., Jarfors, A.E.W., Aue-u-lan, Y., Castagne, S., 2010. Formability in AA5083 and AA6061 alloys for light weight applications. Mater. Des. 31, S66–S70.

Liu, S., Chao, Y.J., 2005. Determination of global mechanical response of friction stir welded plates using local constitutive properties. Modell. Simul. Mater. Sci. Eng. 13, 1–15.

Lockwood, W.D., Reynolds, A.P., 2003. Simulation of the global response of a friction stir weld using local constitutive behavior. Mater. Sci. Eng. A 339, 35–42.

Lockwood, W.D., Tomaz, B., Reynolds, A.P., 2002. Mechanical response of friction stir welded AA2024: experiment and modeling. Mater. Sci. Eng. A 323, 348–353.

Mahoney, M.W., Rhodes, C.G., Flintoff, J.G., Bingel, W.H., Spurling, R.A., 1998. Properties of friction-stir-welded 7075 T651 aluminum. Metall. Mater. Trans. A 29, 1955–1964.

Miles, M.P., Nelson, T.W., Decker, B.J., 2004. Formability and strength of friction-stir-welded aluminum sheets. Metall. Mater. Trans. A 35, 3461–3468.

Miller, W.S., Zhuang, L., Bottema, J., Wittebrood, A.J., De Smet, P., Haszler, A., Vieregge, A., 2000. Recent development in aluminium alloys for the automotive industry. Mater. Sci. Eng. A 280, 37–49.

Mohamed, M.S., Foster, A.D., Lin, J., Balint, D.S., Dean, T.A., 2012. Investigation of deformation and failure features in hot stamping of AA6082: experimentation and modelling. Int. J. Mach. Tool Manuf. 53, 27–38.

Ren, S.R., Ma, Z.Y., Chen, L.Q., 2007. Effect of welding parameters on tensile properties and fracture behavior of friction stir welded Al–Mg–Si alloy. Scr. Mater. 56, 69–72.

Tarng, Y.S., Tsai, H.L., Yeh, S.S., 1999. Modeling, optimization and classification of weld quality in tungsten inert gas welding. Int. J. Mach. Tool Manuf. 39, 1427–1438.

Toros, S., Ozturk, F., Kacar, I., 2008. Review of warm forming of aluminum–magnesium alloys. J. Mater. Process Tech. 207, 1–12.

Watanabe, T., Takayama, H., Yanagisawa, A., 2006. Joining of aluminum alloy to steel by friction stir welding. J. Mater. Process Tech. 178, 342–349.

Zadpoor, A.A., Sinke, J., Benedictus, R., 2007. Mechanics of tailor welded blanks: an overview. Key Eng. Mater. 344, 373–382.